Application of the Strain Energy Density criterion for Patient-Specific Bone Remodeling Simulation

Tingyu Dai , Robin Reinardt , Michael Roland , Stefan Diebels , Bergita Ganse , Marcel Orth , Gargi Shankar Nayak *

Posted Date: 24 March 2026

doi: 10.20944/preprints202603.1884.v1

Keywords: strain energy density; bone remodeling; digital medicine; fracture healing

 doi:10.20944/preprints202603.1884.v1

Article

Application of the Strain Energy Density Criterion for Patient-Specific Bone Remodeling Simulation

Tingyu Dai [1], Robin Reinardt [1], Michael Roland [1], Stefan Diebels [1], Bergita Ganse [2], Marcel Orth [3] and Gargi Shankar Nayak [1,4,5,*]

[1] Chair of Applied Mechanics, Saarland University, Campus A4 2, 66123 Saarbrücken, Germany
[2] Werner Siemens Endowed Chair of Innovative Implant Development (Fracture Healing), Saarland University, Kirrberger Str. 1, bld. 57, 66421 Homburg, Germany
[3] Department of Trauma, Hand and Reconstructive Surgery, Departments and Institutes of Surgery, Saarland University, Homburg, Germany
[4] Bio-Mechanics & Materials group, Department of Head and Neck Medicine, University Medical Center of the Johannes Gutenberg-University Mainz, 55131 Mainz, Germany
[5] Platform for Biomaterial Research, BiomaTiCS group, University Medical Center of the Johannes Gutenberg University Mainz, Mainz, Germany
* Correspondance: gargi.nayak@uni-mainz.de

Abstract

Strain energy density-based algorithms are widely applied in modelling bone healing, yet their use under patient-specific conditions remains underdeveloped. This study aims not only to perform patient-specific bone healing simulations, but specifically to identify which postoperative loading condition provides the most favourable mechanical environment for callus remodeling and thus supports optimal fracture healing. Using postoperative radiographic data of a 63-year-old male patient with a distal diaphyseal tibial fracture and concomitant proximal and distal fibular fractures, a three-dimensional finite element model of the tibia was reconstructed, imported into a multiphysics simulation environment, and coupled with an iterative numerical algorithm. An initial uniform callus density of 750 kg/m^3 was assigned to represent the later stage of secondary healing. The effects of different mechanical loading conditions (partial weight-bearing, physiological loading, and supraphysiological loading) on the mechanical response and density evolution of the callus were evaluated. Partial weight-bearing resulted in insufficient mechanical stimulation and progressive density loss within the callus. Physiological loading generated strain energy density levels consistent with known osteogenic ranges and promoted continuous cortical shell formation and overall density increase. Supraphysiological loading led to overload-related resorption and spatial heterogeneity, ultimately compromising callus stability. The findings demonstrate that loading magnitude significantly influences bone healing. Depending on the healing stage, an optimal load can be determined to minimize the risk of non-union formation and enhance bone remodeling via this methodology. Furthermore, by additionally evaluating unphysiological overloading, this study provides a more robust validation of the model's behaviour outside the optimal mechanobiological window.

Keywords: strain energy density; bone remodeling; digital medicine; fracture healing

1. Introduction

Despite advancements in medical technology, fracture non-union remains a significant clinical challenge. Fracture non-union is generally defined as a fracture that fails to unite within at least six months after the initial injury or shows no visible progression toward healing over a three-month period [1]. For instance, tibial fractures exhibit a non-union rate of approximately 14% [2]. Non-union incurs high socioeconomic costs [3], and it can lead to limitations in ambulation, chronic pain,

 doi:10.20944/preprints202603.1884.v1

reduced ability to participate in occupational and social activities, and a diminished health-related quality of life [4].

However, addressing these issues is demanding, as optimal fracture treatment requires to consider biomechanical (fracture stability) and biological factors alike [5]. Attempting full weight-bearing with inadequate fractured bone strength may inhibit and prolong the healing process [6]. Conversely, inadequate mechanical loading likewise has a negative influence and may delay the healing process [7]. Thus, defining the treatment strategy that can determine the optimal loading range based on the healing conditions of the patient can be of great interest for clinicians. At present, recommendations regarding the type and dose of weight-bearing activity after lower limb fractures are still largely based on empirical evidence rather than reproducible biomechanical data, partly because the mechanical environment that optimally supports bone healing remains insufficiently characterized [8]. Although patients cannot precisely control the loads transmitted through the injured limb during daily activities [9,10], such information is increasingly relevant for the design and evaluation of emerging smart implants with active actuation capabilities. These implant concepts rely on a detailed understanding of load-dependent healing stimuli to adaptively modulate the mechanical environment around the fracture [11].

One of the most influential concepts for describing the relationship between mechanical loading and bone adaptation is Frost's Mechanostat theory [12]. This theory states that specific mechanical strain thresholds, which are tissue specific, govern bone adaptation; different skeletal structural tissues, such as cortical bone, trabecular bone, cartilage, and ligaments, have distinct threshold values due to their biological and mechanical properties. Strains below the lower threshold (disuse window) trigger bone resorption and reduce bone mass; strains within the intermediate range (adapted or lazy zone) maintain bone mass and architecture with minimal remodeling; strains above the upper modelling threshold stimulate bone formation, increasing strength and mass; and strains beyond the pathological overload threshold cause microdamage, triggering repair-related remodeling [12]. This threshold-based concept guides the definition of loading conditions that facilitate bone healing and prevent damage from excessive strain. On tissue level, mechanosignalling [13] is key for these tissue adaptation processes.

Over the past decades, simulation technologies have attracted increasing attention as innovative tools in fracture treatment research [14–17]. Generally, mechanobiological models based on tissue differentiation theories are used to model the initial bone healing phase, whereas strain energy density (SED) based models are applied to model the bone remodeling process [18–21]. However, in the recent past Celik et al. developed a computational framework using SED as a key parameter to model bone remodeling around dental implants during the healing period [22,23]. While this study demonstrated the utility of SED as a mechanobiological stimulus and provided insights into long-term bone density changes under cyclic loading, its scope was limited to idealized, non-patient-specific scenarios. Such simplifications restrict their applicability to real-world clinical cases where variability in patient anatomy, weight-bearing conditions, implant positioning and tissue properties significantly influence the fracture healing scenario.

To address these limitations, the present study aims to develop a finite element (FE) model based on three-dimensional (3D) bone data derived from real patient computed tomography (CT) images.

2. Materials and Methods

2.1. SED-Based Healing Algorithm

The mechanical stimulus for bone remodeling was approximated by SED (U) / density (ρ), representing the SED per unit bone mass. Here, U is site-specific, meaning that its value varies depending on the location within the bone [24]. In this study, the callus was assigned as the initial material property in the FE model. During the simulation, after each loading step, the change in density was calculated using the algorithm proposed by J. Li et al. [25], see Equation (1). The updated density was then assigned as the material property for the next iteration step, thereby driving the

 doi:10.20944/preprints202603.1884.v1

bone remodeling process. In this algorithm, the equation's roots, defined as k and B/D+k, serve as critical thresholds that classify the mechanical stimulus into three distinct regions: under-load resorption, bone growth, and overload resorption. By adjusting the parameters B, D, and k, the model can be tailored to different bone types. Furthermore, the "lazy zone" concept defines a range of mechanical stimuli, ((1 − w)k, (1 + w)k), within which no remodeling occurs:

$$\frac{d\rho}{dt} = \begin{cases} 0 & ,if\ \frac{u}{\rho}\epsilon[(1-w)k,(1+w)k] \\ B\left(\frac{U}{\rho}-k\right) - D\left(\frac{U}{\rho}-k\right)^2, & otherwise \end{cases} \quad (1)$$

where w (width of the lazy zone) was set to 0.2, B was set to 1.0 $(g.cm^{-3})^2 MPa^{-1}$ $(time\ unit)^{-1}$, and D was set to 60 $(g.cm^{-3})^2 MPa^{-2}$ $(time\ unit)^{-1}$. The value of k was calibrated represent the callus tissue type as 0.0004 (J/g) [22].

The Young's modulus (E) was related to ρ via empirical power-law relationship given by Carter et al. [26]:

$$E(\rho) = C\rho^3 \quad (2)$$

where C = 3790 MPa $(g\ cm^{-3})^{-3}$ is a material constant. After each remodeling iteration (time step), the relationship for every element was determined, and the FE model was subsequently updated to reflect the corresponding changes in material properties. Based on Young's modulus, the bone tissue within the callus was classified into three categories: regions with modulus below 5 GPa were considered as non-mineralized tissue (no bone generation), those between 5-16 GPa were defined as trabecular bone, and those between 16-20 GPa were defined as cortical bone [27–29].

2.2. Patient-Specific Model Development

This This study investigated the case reported by Orth et al. of a 63-year-old male, height 180 cm and weight 95 kg, who sustained fractures of the tibia and the proximal as well as distal end of the fibula [30]. The patient underwent an initial closed reduction stabilized with an external fixator, followed by intramedullary nailing of the tibia and plate osteosynthesis of the distal fibular fracture. This study focused on analysing the sensitivity of bone remodeling in a patient who, after six weeks postoperative with approximately 35% body weight (BW) loading, was subsequently allowed to progress to full weight-bearing as recommended by the surgeon. A 3D tibial model was reconstructed from CT data using Synopsys Simpleware™ software (Synopsys, Inc., Sunnyvale, USA), a specialized platform for converting medical imaging datasets into high-quality computational models. Semi-automatic segmentation was performed to distinguish cortical bone, trabecular bone, orthopedic implants, and fracture gaps, followed by manual refinement together with the treating surgeon to ensure anatomical accuracy. The study focused exclusively on the tibia and the fracture callus, excluding the fibula from the analysis. The segmented 3D reconstruction is shown in Figure 1, where the tibia is depicted in grey, the fracture callus in red, and the orthopedic implants and screws in brown. Although the full tibial geometry was included in the FE model to ensure realistic load transfer, only the callus region was considered for the evaluation of material properties in the simulations.

A high-resolution FE mesh was generated using quadratic tetrahedral elements, comprising 79,218 elements for the implant, 41,766 for the callus, and 244,072 for the bone, thereby balancing computational efficiency and numerical accuracy. Cortical and trabecular bone were differentiated using a grey value threshold derived from the CT data. Based on this classification, material properties were assigned assuming linear elastic, isotropic behavior. Cortical bone was assigned a Young's modulus of 18 GPa and a Poisson's ratio of 0.30, while trabecular bone was assigned a Young's modulus of 7.5 GPa and a Poisson's ratio of 0.30. The callus with properties of 750 kg/m^3 and 1.6 GPa. The selected Young's modulus values fall within the range reported in the literature for cortical and trabecular bone [27–29]. The orthopedic implant and screws were modeled as titanium

 doi:10.20944/preprints202603.1884.v1

alloy with a Young's modulus of 108 GPa and a Poisson's ratio of 0.37, consistent with previously reported material properties of Ti-based implants [18].

The meshed model was imported into COMSOL Multiphysics® software, where boundary conditions and physiological loading were defined. Boundary conditions were defined to represent physiological load transfer during gait. The distal end of the tibia was fully constrained in all translational and rotational degrees of freedom, representing the mechanical support provided by the ankle joint. At the proximal tibia, external forces were applied to simulate joint contact loading during walking. The load was decomposed into three orthogonal components (X, Y, Z), corresponding to the medial–lateral, anterior–posterior, and distal–proximal directions, respectively, as illustrated in Figure 1b. This loading configuration was derived from in vivo measurements reported in the Orthoload database [31], ensuring physiological relevance of the applied boundary conditions. The loading conditions were derived from the Orthoload database, which provides in vivo knee joint contact forces during level walking [32]. In this dataset, the peak knee joint contact force reached approximately -251% BW along the z-axis, while the forces along the x- and y-axes were considerably smaller (0.2% and 0.3% BW, respectively). These force magnitudes reflect the combined effects of ground reaction forces and muscle actions during normal gait. In this study, the peak resultant force from Orthoload was defined as the physiological reference load, and the applied loading scenarios (35%, 100%, and 200%) were expressed as percentages of this reference load. Here, 35% served as a partial weight-bearing, 100% corresponded to physiological loading during normal walking, and 200% represented supraphysiological overloading. The x-, y-, and z-directions were assigned to the medial–lateral, anterior–posterior, and distal–proximal axes of the tibia, respectively. The z-directional peak corresponds to the moment when the contralateral leg lifts off during gait, whereas characteristic x- and y-directional peaks occur near foot flat, heel strike, and toe-off.

For the FE analysis, the axial load at contralateral leg lift-off, together with its corresponding x- and y-components, was applied to the proximal tibia. The callus was subsequently loaded with 35%, 100%, and 200% of the physiological reference load to investigate its remodeling response under reduced, physiological, and elevated loading conditions. Each simulation was iterated for 300 remodeling steps. The simulations were performed solely on the tibial 3D model. As the fibula contributes to load sharing, its omission may slightly overestimate the mechanical demand borne by the tibia.

An iterative MATLAB R2022a algorithm, implemented via COMSOL LiveLink™ for MATLAB, automated the simulation by updating density-dependent material properties of the callus, recalculating SED distributions, and repeating the FE analysis until convergence.

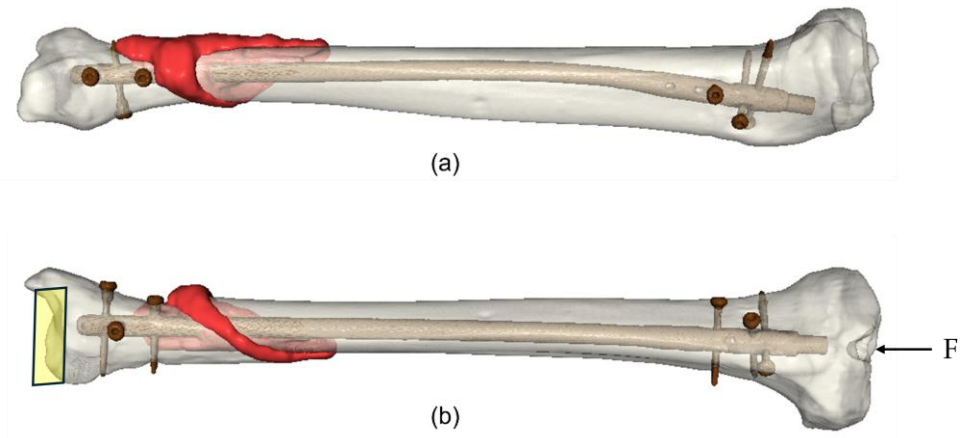

Figure 1. Segmented 3D reconstruction of the post-operative tibial model**.** (**a**) Medial–lateral view of the tibia. (**b**) Anterior–posterior view of the tibia.

 doi:10.20944/preprints202603.1884.v1

2.3. Bone Remodeling Algorithm

As an initial callus, was employed in the simulations to investigate the influence of mechanical stimuli on bone resorption and formation. The simulation methodology can be seen in Figure 2.

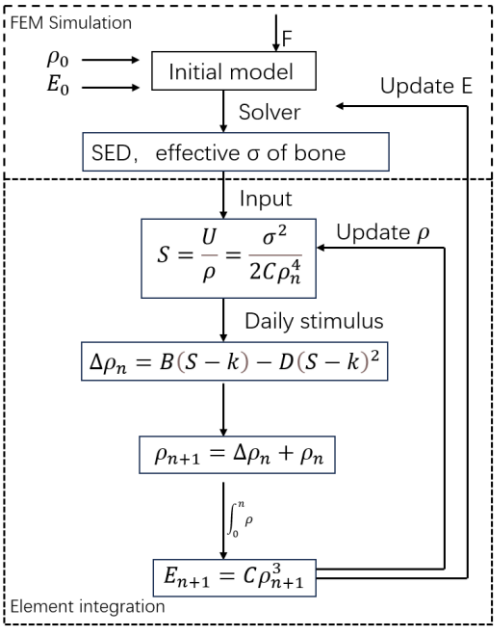

Figure 2. Outline of the bone-remodeling algorithm used in FE model analysis. Modified from Hasan [15].

To ensure numerical stability and prevent non-physiological changes in bone density, constraints were applied. The maximum permissible change in bone density per iteration was restricted to 20 kg/m^3, mitigating abrupt, unrealistic fluctuations. Additionally, a minimum density threshold of 10 kg/m^3 was imposed to prevent numerical collapse, ensuring the integrity of the simulation. The maximum density was capped at 1740 kg/m^3, corresponding to the range from soft tissue to fully mineralized cortical bone, as reported in previous studies [22].

3. Results

Simulations under varying loading levels revealed pronounced differences in the SED distribution during callus remodeling (Figure 3). Following the classification algorithm proposed by J. Li et al. [25], the mechanical stimulus can be divided into four regions: underload resorption (red), lazy zone (blue), bone formation (green), and overload resorption (yellow). These findings clearly demonstrate that the healing callus exhibits a distinct load-dependent response. The physiological loading condition produced the most favorable mechanical environment for consolidation, whereas both partial weight-bearing and supraphysiological loading shifted many elements outside the optimal Mechanostat window, thereby compromising the remodeling process.

Under the first loading cycle, the initial callus exhibited SED ranges of 0.0004–36.8J/kg under partial weight-bearing, 0.003–268 J/kg physiological loading, and 0.01–1075 J/kg under supraphysiological loading. As the applied load increased, both the minimum and maximum SED values rose by several orders of magnitude, demonstrating a clear load-dependent scaling of the mechanical stimulus within the callus. The SED range obtained under the physiological loading conditions agrees well with the FE bone remodeling model of Weinans et al. [33], which reported reference values of approximately 4 J/kg for the femoral shaft and 250 J/kg for an idealized cortical plate. This agreement suggests that the physiological loading condition provides a mechanically relevant stimulus for callus remodeling. In contrast, values under the partial weight-bearing condition are largely below this optimal range, whereas those under supraphysiological substantially exceed it— both of which are unfavourable for consolidation.

 doi:10.20944/preprints202603.1884.v1

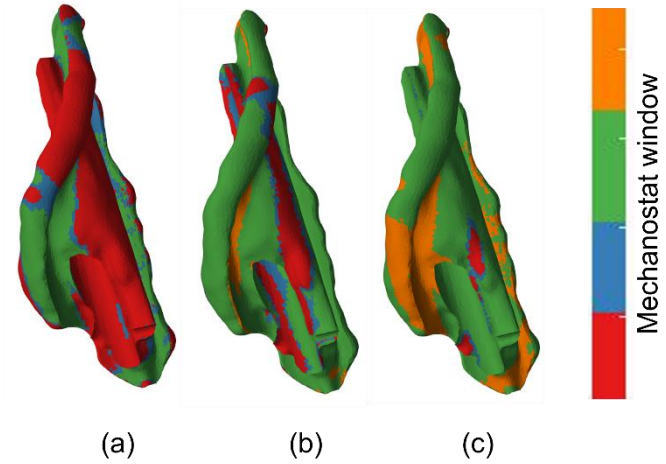

Figure 3. Distribution of SED within the initial callus under (a) partial weight-bearing, (b) physiological loading, and (c) supraphysiological loading. Under partial weight-bearing, most elements fell within the underload resorption region, with only limited bone formation, indicating insufficient mechanical stimulation for callus consolidation. Under physiological loading, the majority of elements were located in the bone formation zone, representing the most favourable mechanical condition for secondary healing. Under supraphysiological loading, however, a substantial proportion of elements exceeded the overload threshold, particularly in the peripheral callus regions, where resorption dominated despite the presence of some bone-forming areas.

Based on the SED-driven remodeling algorithm, the callus density evolution corresponded directly to variations in the SED distribution**.** When the fully healed callus was subjected to partial weight-bearing, representing the first six postoperative weeks, the density gradually decreased throughout the remodeling process. After 300 remodeling iterations, a widespread reduction in density (red regions) was observed, as shown in Figure 4a. In contrast, when the applied load was increased to physiological loading, as recommended by the surgeon after the first six weeks postoperatively, the callus density exhibited a clear upward trend, with extensive regions of density gain (green areas), indicating a significant improvement in bone remodeling, as illustrated in Figure 4b. However, under supraphysiological loading, most regions once again demonstrated a sharp decline in density, reflecting overload-induced resorption, as shown in Figure 4c.

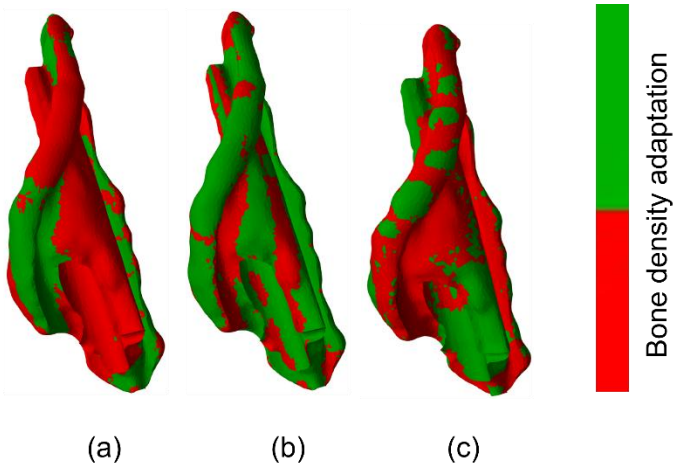

Figure 4. Distribution of callus density after 300 remodeling iterations under different loading conditions: (**a**) partial weight-bearing, (**b**) physiological loading, and (**c**) supraphysiological loading. Green regions represent bone formation associated with adequate mechanical stimulation, whereas red regions indicate density loss caused by either insufficient loading or overload-induced resorption.

 doi:10.20944/preprints202603.1884.v1

As shown in Figure 5, cortical bone gradually formed under both physiological loading and supraphysiological loading; however, the spatial distribution of newly formed cortical bone differed between the two cases.

Under reduced loading, the callus mainly consisted of low-density tissue, indicating that the mechanical stimulus was insufficient to induce ossification. Under physiological loading, a continuous cortical layer and a well-developed trabecular network were formed, suggesting that the tissue had progressed to a more advanced stage of maturation. Under supraphysiological loading, the callus exhibited pronounced spatial heterogeneity, with discontinuous and fragmented cortical structures that failed to provide adequate mechanical stability to the construct.

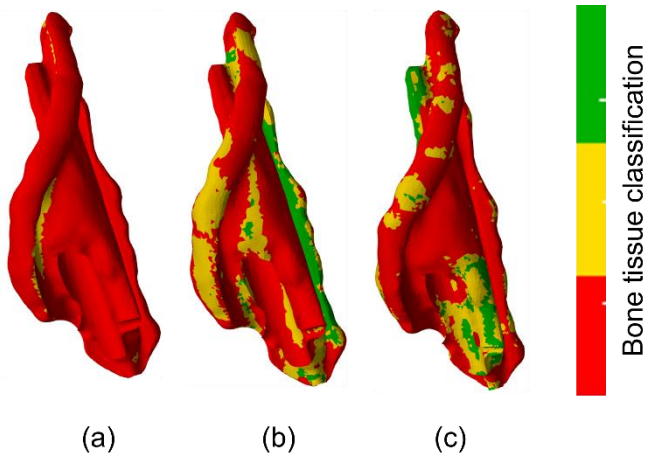

Figure 5. Distribution of tissue types within the callus after 300 remodeling iterations under different loading conditions: (**a**) partial weight-bearing, (**b**) physiological loading, and (**c**) supraphysiological loading. Elements were classified according to Young's modulus thresholds: no bone (< 5 GPa, red), trabecular bone (5–16 GPa, yellow), and cortical bone (16–20 GPa, green). Under partial weight-bearing, the callus predominantly comprised low-density regions with limited trabecular formation. Under physiological loading, a continuous cortical shell and interconnected trabecular network developed, indicating enhanced tissue maturation. Under supraphysiological loading, fragmented cortical structures and a heterogeneous spatial distribution appeared, particularly near the periphery, reducing overall structural stability.

To better visualize the distribution of bone tissue around the fracture fragments, the callus was sectioned along the medial–lateral and anterior–posterior planes, and the results were compared with the postoperative X-ray images obtained seven months postoperatively. Figure 6b shows the slice of the initial callus with a uniform Young's modulus of 1.6 GPa, representing the first six weeks after surgery. Figure 6c depicts the same region after 300 remodeling iterations under physiological loading, where the tissue classification reveals the differentiation of the callus into trabecular and cortical bone. The figure provides a magnified view of the region (in red) shown in Figure 6b, illustrating local mineralization and tissue maturation along the fracture margins.

In the postoperative CT scan (Figure 6a), a clear interfragmentary gap can still be observed between the fracture fragments, indicating incomplete consolidation during the early healing phase. In contrast, the X-ray image obtained seven months after surgery (Figure 6d) shows complete posterior bridging of the fracture gap, while the anterior region remains partially filled with immature trabecular bone of relatively low radiodensity. This observation aligns closely with the simulation results, which also demonstrate asymmetrical bone formation—dense cortical bone forming along the posterior and outer cortical regions that connect the fragments, whereas in the anterior view, trabecular bone occupies a broad region, but cortical bone formation remains incomplete.

 doi:10.20944/preprints202603.1884.v1

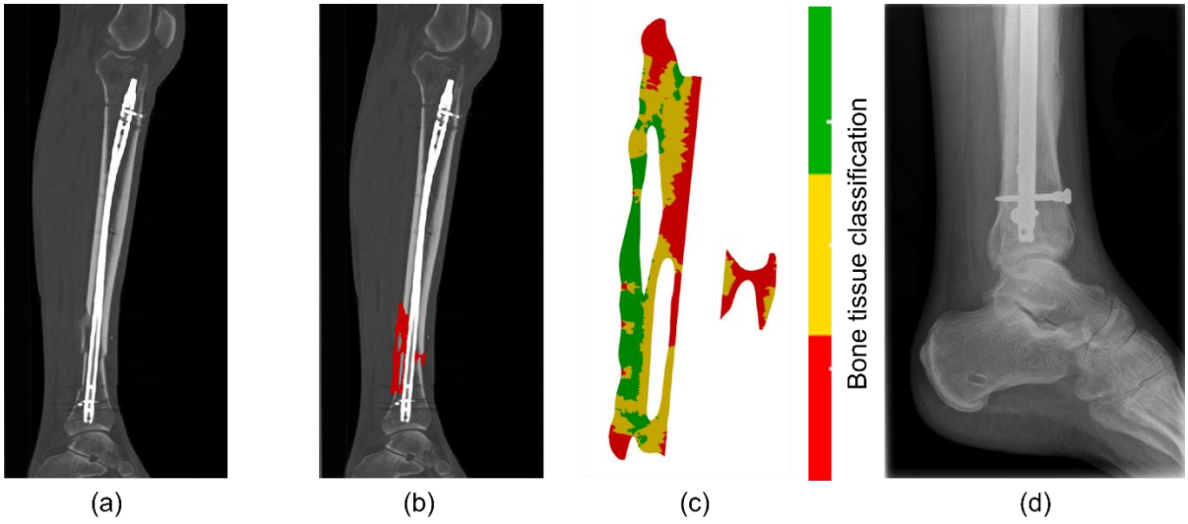

Figure 6. Comparison between clinical imaging and simulation results from the medial–lateral view. (**a**,**b**) Postoperative CT scans of the tibia showing the fixation implant in place and the segmented callus region highlighted in red. (**c**) The result of FE simulation displaying lateral slices of the callus after 300 remodeling iterations under physiological loading, illustrating tissue classification where red, yellow, and green represent non-mineralized tissue, trabecular bone, and cortical bone, respectively. (d) Postoperative X-ray image demonstrating full weight-bearing with intramedullary nail fixation in situ.

When examining the anterior–posterior view of the X-ray (Figure 7d), it becomes apparent that the outer regions protruding from the bone are not yet fully mineralized, and the fracture gap in this view is not filled with high-density bone. The simulation supports these findings (Figure 7c), showing low-density regions at the periphery and a fracture gap filled only with trabecular bone. This further demonstrates the model's potential to predict the actual spatial evolution of the callus, which over time is expected to remodel toward the original bone shape. The strong correspondence between the simulation and the clinical imaging supports the validity of the SED-based remodeling framework in predicting spatially heterogeneous healing patterns.

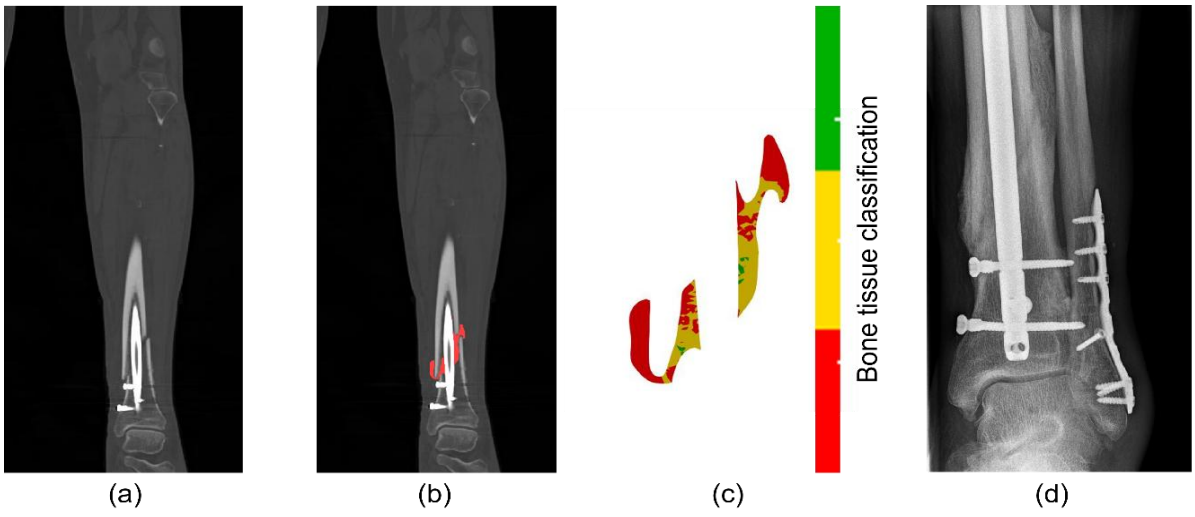

Figure 7. Comparison between clinical imaging and simulation results from the anterior-posterior view. (**a**,**b**) Postoperative CT scans showing the fixation implant and the segmented callus region highlighted in red. (**c**) The result of FE simulation displaying anterior-posterior slices of the callus after 300 remodeling iterations under physiological loading, illustrating tissue classification where red, yellow, and green represent non-mineralized tissue, trabecular bone, and cortical bone, respectively. (**d**) Postoperative X-ray image obtained seven months after surgery showing satisfactory bone healing with the fixation in place.

 doi:10.20944/preprints202603.1884.v1

4. Discussion and Conclusions

This study developed and validated a patient-specific SED-based model for bone remodeling through FE analysis. The model successfully simulates the adaptive responses of bone tissue under varying mechanical stimuli, providing insights into the impact of loading conditions on fracture healing. By integrating patient-specific anatomical structures, individualized tissue properties, and personalized weight-bearing conditions, the model offers a more clinically relevant representation of the fracture healing process. SED remains a central parameter, but its integration is enhanced by considering dynamic mechanical environments and heterogeneous callus states that reflect the actual variability in the patient's conditions.

The results demonstrated that bone remodeling within the callus is highly sensitive to external mechanical loading, previous mechanobiological findings showing that tissue differentiation and repair outcomes depend strongly on the timing and magnitude of mechanical stimulation during healing [34]. In the fully healed callus, partial weight-bearing conditions provided insufficient mechanical stimulation to sustain bone formation, leading to a gradual reduction in density dominated by resorptive activity. Under physiological loading conditions, the SED distribution and density evolution indicated an optimal mechanical environment that facilitated the formation of a continuous cortical shell and enhanced structural consolidation. In contrast, supraphysiological loading induced pronounced overload-related resorption and spatial heterogeneity within the callus, ultimately compromising its overall mechanical stability.

The classification of tissue types further confirmed that appropriate mechanical loading promotes the transition of the callus from low-density tissue to mature cortical bone, whereas both insufficient and excessive loading impede ossification. The simulated spatial distribution of bone tissue corresponded closely with postoperative radiographs, validating the predictive accuracy of the SED-based FE model.

Within the present framework, the cubic density–modulus relationship proposed by Carter et al. implies that the mass-specific mechanical stimulus scales with ρ^3, ε^2. As callus density and stiffness increase, strain under a given load decreases, such that higher external forces are required to maintain the target SED. This mechanism explains the observed trend in our simulation, where the required loading during the soft callus phase in the first six postoperative weeks was approximately partial weight-bearing conditions, and increased to around full weight-bearing conditions during the hard callus phase after six weeks. This finding is consistent with the clinical strategy of staged loading (dynamisation). Experimental studies support this trend. Gardner et al. applied cyclic axial compression to healing mouse tibiae and found that higher forces were needed at later healing stages to enhance callus stiffness, whereas Mehta et al. reported increased callus volume and mineralisation when semi rigid fixation allowed greater interfragmentary motion in young, but not aged, rats [35,36]. Although neither study quantified SED directly, their outcomes suggest that the osteogenic load must rise as the regenerate stiffens.

The numerical SED values reported here remain contingent on the adopted density modulus law; alternative ρ-E relationships would shift the absolute window, but the relative state dependence should persist. Expressing results in both external and internal SED terms facilitates cross study comparison and translation to fixation design. Putative biological modifiers such as age, vascularity and systemic disease were deliberately held constant in the present analysis and merit explicit inclusion in future work.

It must be noted, however, that truly uniaxial compression is uncommon in vivo. Because the tibial shaft is gently curved, any small lateral offset of the joint reaction force generates an additional bending moment that places the anterior cortex in tension and the posterior cortex in compression. Cadaver experiments have shown that such bending can govern the failure location even when the external load is nominally axial [37]. This observation is consistent with material level data. Cortical bone is only about 10–30% stronger in compression than in tension, so tensile stresses on the convex side of the bent shaft often set the functional strength limit [38].

 doi:10.20944/preprints202603.1884.v1

From a mechanobiological perspective, the optimal stimulus for fracture healing is therefore one of predominant axial compression coupled with low but not zero bending and shear. Experimental osteotomy models demonstrate that small cyclic axial micromotions (≈ 1–3% gap strain) accelerate callus maturation, whereas large shear or bending amplitudes delay union [36,39]. Contemporary fixation systems accordingly aim to bias load transfer towards compression while constraining excessive rotation and flexure. The present findings, which isolate the osteogenic potency of pure z-axis loading, reinforce this design philosophy but also underscore the necessity to account for inevitable off-axis components when translating numerical predictions into clinical protocols.

However, while the SED-based model performs well in simulating mechanical adaptability, its simplified mechanical framework overlooks biological factors such as cellular activity and biochemical signals. To improve the model's accuracy, future research should incorporate biological processes (e.g., osteoblast proliferation, osteoclast activity, and further stem cell differentiation) into the framework. Moreover, this model has not included the treatment of the double-fractured fibula and its osteosynthesis of the distal fracture, as this concomitant fracture may have affected the healing of this complex injury of the lower leg (as e.g., the necessity to obtain partial weight-bearing for the first six weeks postoperatively). Combining FE analysis with biological simulations could enhance the predictive capability of the model, leading to better clinical strategies for fracture repair.

As a limitation, the present study only used a single patient case for simulation to show technical feasibility. To derive generalizable findings of weight-bearing scenarios, that are generally valid for most patients, a group of patients with varying fracture types, sexes and age groups would need to be studied. Therefore, the results presented here may not be transferable to other patients. Furthermore, the simulation only considers biomechanical aspects of fracture healing, while many nonunion cases are caused by insufficiencies on biological level, such as a diminished blood supply [3]. Another limitation is that the mechanical pull of skeletal muscles was ignored in this simulation. However, this pull is known to add deformation to the bone, e.g., torsion of the tibia during push-off [40,41]. In addition, a limitation of this workflow is that it cannot be immediately applied in the daily clinical context due to its complexity. Automated software solutions would need to be developed to allow clinicians to actually use these simulations in their daily work. It is, however, a valuable asset for fracture healing research.

In summary, the results emphasize the importance of applying appropriate mechanical forces in bone healing and demonstrate the potential of SED-based models in deepening the understanding of bone remodeling. By combining patient-specific data with advanced simulation techniques, the model provides a comprehensive perspective on the dynamic mechanisms underlying fracture healing. The findings aim to mitigate complications, optimize recovery outcomes for complex fractures, and ultimately improve clinical prognoses. This study seeks to bridge the gap between theoretical simulations and their practical application in personalized medicine. However, further development is needed to integrate the biological complexities, which will pave the way for more accurate and comprehensive predictions of bone healing and treatment strategies.

Authors Contribution: G.S.N., M.R. and S.D.; Formal analysis: T.D., G.S.N., M.R., S.D., R.R., B.G. and M.O.; Funding acquisition: B.G., S.D. and G.S.N.; Investigation: T.D.; Methodology: T.D., G.S.N., R.R. and M.R.; Supervision: G.S.N., M.R. and S.D.; Writing—original draft preparation: T.D.; Writing—review and editing: G.S.N., M.R., R.R., S.D., B.G. and M.O. All authors have read and agreed to the published version of the manuscript.

Funding: This study was partly funded by the Werner Siemens Foundation under the grant "Smart Implants 2.0".

Institutional Review Board Statement: Ethical approval was obtained from the IRB of Saarland Medical Board (Aerztekammer des Saarlandes, Germany, application number 30/21). Informed consent was conducted according to the Declaration of Helsinki. The study is part of the project Smart Implants 2.0—Weight-bearing and Gait Observation for Early Monitoring of Fracture Healing and Individualized Therapy after Trauma,

 doi:10.20944/preprints202603.1884.v1

funded by the Werner Siemens Foundation. It is registered in the German Clinical Trials Register (DRKS-ID: DRKS00025108).

Data Availability Statement: Due to personal data protection laws, the datasets used in this study cannot be shared with external researchers.

Conflicts of Interest: The authors declare no conflict of interest.

Clinical Trial Number: Not applicable.

Abbreviations

The following abbreviations are used in this manuscript:

SED	Strain Energy Density
FE	Finite Element
FEM	Finite Element Method
CT	Computed Tomography
BW	Body Weight

References

1. Nicholson, J.A.; Makaram, N.; Simpson, A.; Keating, J.F. Fracture nonunion in long bones: A literature review of risk factors and surgical management. *Injury* **2021**, *52*(Suppl 2), S3–S11. https://doi.org/10.1016/j.injury.2020.11.029.
2. Zura, R.; Xiong, Z.; Einhorn, T.; Watson, J.T.; Ostrum, R.F.; Prayson, M.J.; De La Rocca, G.J.; Mehta, S.; McKinley, T.; Wang, Z.; Steen, R.G. Epidemiology of fracture nonunion in 18 human bones. *JAMA Surg.* **2016**, *151*(11), e162775. https://doi.org/10.1001/jamasurg.2016.2775.
3. Zura, R.; Xiong, Z.; Einhorn, T.; Watson, J.T.; Ostrum, R.F.; Prayson, M.J.; De La Rocca, G.J.; Mehta, S.; McKinley, T.; Wang, Z.; Steen, R.G. Epidemiology of fracture nonunion in 18 human bones. *JAMA Surg.* **2016**, *151*(11), e162775. https://doi.org/10.1001/jamasurg.2016.2775.
4. Brinker, M.R.; Hanus, B.D.; Sen, M.; O'Connor, D.P. The devastating effects of tibial nonunion on health-related quality of life. *J. Bone Joint Surg. Am.* **2013**, *95*(24), 2170–2176. https://doi.org/10.2106/JBJS.L.00803.
5. Ulstrup, A.K. Biomechanical concepts of fracture healing in weight-bearing long bones. *Acta Orthop. Belg.* **2008**, *74*(3), 291–302.
6. Augat, P.; Merk, J.; Ignatius, A.; Margevicius, K.; Bauer, G.; Rosenbaum, D.; Claes, L. Early, full weight-bearing with flexible fixation delays fracture healing. *Clin. Orthop. Relat. Res.* **1996**, *328*, 194–202. https://doi.org/10.1097/00003086-199607000-00031.
7. Mavčič, B.; Antolič, V. Optimal mechanical environment of the healing bone fracture/osteotomy. *Int. Orthop.* **2012**, *36*(4), 689–695. https://doi.org/10.1007/s00264-012-1487-8.
8. Zhang, L.; Miramini, S.; Richardson, M.; Ebeling, P.; Little, D.; Yang, Y.; Huang, Z. Computational modelling of bone fracture healing under partial weight-bearing exercise. *Med. Eng. Phys.* **2017**, *42*, 65–72. https://doi.org/10.1016/j.medengphy.2017.01.025.
9. Ganse, B.; Yang, P.F.; Gardlo, J.; Gauger, P.; Kriechbaumer, A.; Pape, H.C.; Koy, T.; Müller, L.P.; Rittweger, J. Partial weight bearing of the tibia. *Injury* **2016**, *47*(8), 1777–1782. https://doi.org/10.1016/j.injury.2016.06.003.
10. Duda, G.N.; Bartmeyer, B.; Sporrer, S.; Taylor, W.R.; Raschke, M.; Haas, N.P. Does partial weight bearing unload a healing bone in external ring fixation? *Langenbecks Arch. Surg.* **2003**, *388*, 298–304. https://doi.org/10.1007/s00423-003-0386-2.
11. Ganse, B.; Orth, M.; Roland, M.; Diebels, S.; Motzki, P.; Seelecke, S.; Kirsch, S.M.; Welsch, F.; Andres, A.; Wickert, K.; Braun, B.J.; Pohlemann, T. Concepts and clinical aspects of active implants for the treatment of bone fractures. *Acta Biomater.* **2022**, *146*, 1–9. https://doi.org/10.1016/j.actbio.2022.05.001.
12. Frost, H.M. Bone "mass" and the "mechanostat": A proposal. *Anat. Rec.* **1987**, *219*(1), 1–9. https://doi.org/10.1002/ar.1092190104.

 doi:10.20944/preprints202603.1884.v1

13. Chen, N.; Danalache, M.; Liang, C.; Alexander, D.; Umrath, F. Mechanosignaling in osteoporosis: When cells feel the force. *Int. J. Mol. Sci.* **2025**, *26*(9), 4007. https://doi.org/10.3390/ijms26094007.
14. Lacroix, D.; Prendergast, P.J. A mechano-regulation model for tissue differentiation during fracture healing: Analysis of gap size and loading. *J. Biomech.* **2002**, *35*(9), 1163–1171. https://doi.org/10.1016/S0021-9290(02)00086-6.
15. Hasan, I. Computational simulation of trabecular bone distribution around dental implants and the influence of abutment design on the bone reaction for implant-supported fixed prosthesis. *Ph.D. Thesis*, University of Bonn, Bonn, Germany, 2011.
16. Claes, L.E.; Heigele, C.A.; Neidlinger-Wilke, C.; Kaspar, D.; Seidl, W.; Margevicius, K.J.; Augat, P. Effects of mechanical factors on the fracture healing process. *Clin. Orthop. Relat. Res.* **1998**, *355*, S132–S147. https://doi.org/10.1097/00003086-199810001-00015.
17. Jang, I.G.; Kim, I.Y.; Kwak, B.B. Analogy of strain energy density based bone-remodeling algorithm and structural topology optimization. *J. Biomech. Eng.* **2009**, *131*(1), 011012. https://doi.org/10.1115/1.3005202.
18. Nayak, G.S.; Roland, M.; Wiese, B.; Hort, N.; Diebels, S. Influence of implant base material on secondary bone healing: An in silico study. *Comput. Methods Biomech. Biomed. Engin.* **2025**, *28*(11), 1734–1742. https://doi.org/10.1080/10255842.2024.2338121.
19. Checa, S.; Prendergast, P.J. A mechanobiological model for tissue differentiation that includes angiogenesis: A lattice-based modeling approach. *Ann. Biomed. Eng.* **2009**, *37*, 129–145. https://doi.org/10.1007/s10439-008-9594-9.
20. Shefelbine, S.J.; Augat, P.; Claes, L.; Simon, U. Trabecular bone fracture healing simulation with finite element analysis and fuzzy logic. *J. Biomech.* **2005**, *38*(12), 2440–2450. https://doi.org/10.1016/j.jbiomech.2004.10.019.
21. Nutu, E. Interpretation of parameters in strain energy density bone adaptation equation when applied to topology optimization of inert structures. *Mechanika* **2015**, *21*(6), 443–449. https://doi.org/10.5755/j01.mech.21.6.12106.
22. Celik, S. Simulation of bone remodeling process around dental implant during the healing period. *Ph.D. Thesis*, University of Bonn, Bonn, Germany, 2021. https://doi.org/10.13140/RG.2.2.11365.06888.
23. Frost, H.M. The Utah paradigm of skeletal physiology: An overview of its insights for bone, cartilage and collagenous tissue organs. *J. Bone Miner. Metab.* **2000**, *18*, 305–316. https://doi.org/10.1007/s007740070001.
24. Lin, C.L.; Lin, Y.H.; Chang, S.H. Multi-factorial analysis of variables influencing the bone loss of an implant placed in the maxilla: Prediction using FEA and SED bone remodeling algorithm. *J. Biomech.* **2010**, *43*(4), 644–651. https://doi.org/10.1016/j.jbiomech.2009.10.030.
25. Li, J.; Li, H.; Shi, L.; Fok, A.S.L.; Ucer, C.; Devlin, H.; Horner, K.; Silikas, N. A mathematical model for simulating the bone remodeling process under mechanical stimulus. *Dent. Mater.* **2007**, *23*(9), 1073–1078. https://doi.org/10.1016/j.dental.2006.10.004.
26. Carter, D.R. Mechanical loading histories and cortical bone remodeling. *Calcif. Tissue Int.* **1984**, *36*(Suppl 1), S19–S24. https://doi.org/10.1007/BF02406129.
27. Sharir, A.; Barak, M.M.; Shahar, R. Whole bone mechanics and mechanical testing. *Vet. J.* **2008**, *177*(1), 8–17. https://doi.org/10.1016/j.tvjl.2007.09.012.
28. Choi, K.; Kuhn, J.L.; Ciarelli, M.J.; Goldstein, S.A. The elastic moduli of human subchondral, trabecular, and cortical bone tissue and the size-dependency of cortical bone modulus. *J. Biomech.* **1990**, *23*(11), 1103–1113. https://doi.org/10.1016/0021-9290(90)90003-L.
29. Holmes, D.C.; Loftus, J.T. Influence of bone quality on stress distribution for endosseous implants. *J. Oral Implantol.* **1997**, *23*(3), 104–111.
30. Orth, M.; Ganse, B.; Andres, A.; Wickert, K.; Warmerdam, E.; Müller, M.; Diebels, S.; Roland, M.; Pohlemann, T. Simulation-based prediction of bone healing and treatment recommendations for lower leg fractures: Effects of motion, weight-bearing and fibular mechanics. *Front. Bioeng. Biotechnol.* **2023**, *11*, 1067845. https://doi.org/10.3389/fbioe.2023.1067845.
31. Tho, M.H.B.; Mazeran, P.; Kirat, K.E.; Bensamoun, S. Multiscale characterization of human cortical bone. *CMES* **2012**, *87*(6), 557–578. https://doi.org/10.3970/cmes.2012.087.557.

 doi:10.20944/preprints202603.1884.v1

32. Bergmann, G.; Damm, P. OrthoLoad—Database of orthopedic joint loads. Julius Wolff Institute, Berlin Institute of Health at Charité—Universitätsmedizin Berlin, Berlin, Germany, 2008. Available online: http://www.orthoload.com.
33. Weinans, H.; Huiskes, R.; Grootenboer, H.J. The behavior of adaptive bone-remodeling simulation models. *J. Biomech.* **1992**, *25*(12), 1425–1441. https://doi.org/10.1016/0021-9290(92)90056-7.
34. Liu, C.; Carrera, R.; Flamini, V.; Kenny, L.; Cabahug-Zuckerman, P.; George, B.M.; Hunter, D.; Liu, B.; Singh, G.; Leucht, P.; Mann, K.A.; Helms, J.A.; Castillo, A.B. Effects of mechanical loading on cortical defect repair using a novel mechanobiological model of bone healing. *Bone* **2017**, *108*, 145–155. https://doi.org/10.1016/j.bone.2017.12.027.
35. Gardner, M.J.; van der Meulen, M.C.H.; Demetrakopoulos, D.; Wright, T.M.; Myers, E.R.; Bostrom, M.P. In vivo cyclic axial compression affects bone healing in the mouse tibia. *J. Orthop. Res.* **2006**, *24*(8), 1679–1686. https://doi.org/10.1002/jor.20230.
36. Mehta, M.; Strube, P.; Peters, A.; Perka, C.; Hutmacher, D.; Fratzl, P.; Duda, G.N. Influences of age and mechanical stability on volume, microstructure, and mineralization of the fracture callus during bone healing: Is osteoclast activity the key to age-related impaired healing? *Bone* **2010**, *47*(2), 219–228. https://doi.org/10.1016/j.bone.2010.05.029.
37. Funk, J.R.; Rudd, R.W.; Kerrigan, J.R.; Crandall, J.R. The line of action in the tibia during axial compression of the leg. *J. Biomech.* **2007**, *40*(10), 2277–2282. https://doi.org/10.1016/j.jbiomech.2006.10.012.
38. Kemper, A.; McNally, C.; Kennedy, E.; Manoogian, S.; Duma, S. The material properties of human tibia cortical bone in tension and compression: Implications for the tibia index. In *Proceedings of the 20th International Technical Conference on the Enhanced Safety of Vehicles*, Lyon, France, 18–21 June 2007.
39. Claes, L.E.; Heigele, C.A. Magnitudes of local stress and strain along bony surfaces predict the course and type of fracture healing. *J. Biomech.* **1999**, *32*(3), 255–266. https://doi.org/10.1016/S0021-9290(98)00153-5.
40. Yang, P.F.; Kriechbaumer, A.; Albracht, K.; Sanno, M.; Ganse, B.; Koy, T.; Shang, P.; Brüggemann, G.P.; Müller, L.P.; Rittweger, J. On the relationship between tibia torsional deformation and regional muscle contractions in habitual human exercises in vivo. *J. Biomech.* **2015**, *48*(3), 456–464. https://doi.org/10.1016/j.jbiomech.2014.12.031.
41. Yang, P.F.; Sanno, M.; Ganse, B.; Koy, T.; Brüggemann, G.P.; Müller, L.P.; Rittweger, J. Torsion and antero-posterior bending in the in vivo human tibia loading regimes during walking and running. *PLoS ONE* **2014**, *9*(4), e94525. https://doi.org/10.1371/journal.pone.0094525.